Eur. Phys. J. A (2020) 56:51
https://doi.org/10.1140/epja/s10050-020-00044-9

THE EUROPEAN PHYSICAL JOURNAL A

Regular Article - Experimental Physics

Gamow–Teller strength distributions of ^{116}Sb and ^{122}Sb using the (^{3}He, t) charge-exchange reaction

C. A. Douma[1,a], C. Agodi[2], H. Akimune[3], M. Alanssari[4], F. Cappuzzello[2,5], D. Carbone[2], M. Cavallaro[2], G. Colò[6,7], F. Diel[8], H. Ejiri[9], D. Frekers[4], H. Fujita[9], Y. Fujita[9], M. Fujiwara[9], G. Gey[9], M. N. Harakeh[1], K. Hatanaka[9], F. Hattori[3], K. Heguri[3], M. Holl[4], A. Inoue[9], N. Kalantar-Nayestanaki[1], Y. F. Niu[10,11], P. Puppe[4], P. C. Ries[12], A. Tamii[9], V. Werner[12], R. G. T. Zegers[13,14,15], K. Zuber[16]

[1] KVI-CART, University of Groningen, Zernikelaan 25, 9747AA Groningen, The Netherlands
[2] INFN Laboratori Nazionali del Sud, via S. Sofia 62, 95125 Catania, Italy
[3] Konan University, 8 Chome-9-1 Okamoto, Higashinada Ward, Kobe, Hyōgo, Japan
[4] Institüt für Kernphysik, Universität Münster, 48341 Munster, Germany
[5] Dipartimento di Fisica e Astronomia 'Ettore Majorana', Catania University, via S. Sofia 64, 95125 Catania, Italy
[6] Dipartimento di Fisica, Universitá degli Studi di Milano, Via Celoria 16, 20133 Milan, Italy
[7] INFN, Sezione di Milano, Via Celoria 16, 20133 Milan, Italy
[8] Institut für Kernphysik, Universität zu Köln, Albertus-Magnus-Platz, Cologne 50923, Germany
[9] Research Center for Nuclear Physics, Osaka University, Ibaraki, Osaka 567-0047, Japan
[10] School of Nuclear Science and Technology, Lanzhou University, Lanzhou 730000, China
[11] ELI-NP, Horia Hulubei National Institute for Physics and Nuclear Engineering, 30 Reactorului Street, Măgurele, 077125 Bucharest, Romania
[12] Institut für Kernphysik, Technische Universität Darmstadt, Schlossgartenstraße 9, 64289 Darmstadt, Germany
[13] National Superconducting Cyclotron Laboratory, Michigan State University, East Lansing, MI 48824-1321, USA
[14] Department of Physics and Astronomy, Michigan State University, East Lansing, MI 48824, USA
[15] Joint Institute for Nuclear Astrophysics, Michigan State University, East Lansing, MI 48824, USA
[16] Institut für Kern-und Teilchenphysik, TU Dresden, Dresden, Germany

Received: 10 July 2019 / Accepted: 17 November 2019 / Published online: 11 February 2020

Communicated by A. Obertelli

Abstract The Gamow–Teller strength distributions of ^{116}Sb and ^{122}Sb were measured with the ^{116,122}Sn(^{3}He, t)^{116,122}Sb charge-exchange reactions at 140 MeV/u. The measurements were carried out at the Research Center for Nuclear Physics (RCNP) at Osaka University in Osaka, Japan using the Grand Raiden spectrometer. The data were analysed by Multipole-Decomposition Analysis (MDA). The Gamow–Teller strengths summed up to 28 MeV are (38 ± 7)% and (48 ± 6)% of the Ikeda sum rule for ^{116}Sb and ^{122}Sb, respectively, if the quasi-free scattering (QFS) contribution is not subtracted. These percentages are (29 ± 7)% and (35 ± 5)%, respectively, if the QFS contribution is maximally subtracted. These results were compared to those from previous measurements of the same isotopes, to recent measurements of ^{150}Pm, and to a Quasi-particle Random-Phase Approximation (QRPA) calculation with Quasi-Particle Vibration Coupling (QPVC). The data suggest that the true QFS contribution is small for ^{116}Sb, but are inconclusive about whether the QFS contribution is small or significant for ^{122}Sb. Therefore, these data may provide an interesting test for the general quenching phenomenon of the Gamow–Teller Resonance (GTR). However, more research to reveal the nature of the QFS contribution is still needed on both the experimental and the theoretical side.

1 Introduction

Accurate measurements of Gamow–Teller strength distributions find important usage in three sub-fields of nuclear physics: nuclear structure, neutrino physics and nucleosynthesis. To increase our understanding of nuclear structure, the Gamow–Teller strength distribution is often used to obtain information about the nuclear wave function. The Gamow–Teller strength is usually characterised in terms of a B(GT) value, which is defined as

$$\mathrm{B(GT_{\pm})} = \frac{1}{2J_i + 1} \left| \left\langle \Psi_f \left\| \sum_{j=1}^{A} \boldsymbol{\sigma}_j \boldsymbol{\tau}_{\pm,j} \right\| \Psi_i \right\rangle \right|^2 , \qquad (1)$$

[a] e-mail: c.a.douma@rug.nl

where J_i is the total angular momentum of the parent nucleus and Ψ_i (Ψ_f) is the parent (daughter) nuclear wave function [1]. $\boldsymbol{\tau}_{\pm,j}$ is the isospin raising/lowering operator for the jth nucleon [2] and $\boldsymbol{\sigma}_j$ is the spin operator of the jth nucleon, defined in terms of the x, y and z Pauli spin-matrices. The $\pm$ symbol defines whether the isospin z-component is raised or lowered. Raising the isospin z-component corresponds in a nucleus to a $p \rightarrow n$ transition and lowering corresponds to an $n \rightarrow p$ transition (which is equivalent to performing a (^{3}He, t) on that nucleus). B(GT) can be directly extracted from measurable observables [3], and provides the Gamow–Teller strength for the final state in the daughter nucleus.

In neutrino physics, nuclear matrix elements, and especially the Gamow–Teller ones (see Eq. (1)), frequently enter the calculations of $2\nu\beta\beta$-decay (two-neutrino double-beta decay) [4–7]. This information can then be used, together with other nuclear matrix elements [8], to understand the $0\nu\beta\beta$-decay (neutrino-less double-beta decay), which is especially interesting because even a single observation (which has not been seen yet [4]) undeniably results in the conclusion that the neutrino is a Majorana particle [4]. Moreover, such observations provide hints for Grand Unification Theories (GUT), for SuperSymmetry (SUSY) [5,6,9], and for understanding the matter-antimatter asymmetry in the universe [10]. Calculations of the involved matrix elements, and in particular the Gamow–Teller ones, usually contain substantial uncertainties [11–13]. Hence, a direct measurement of $B(GT)$ values serves as a benchmark for theoretical calculations and thus helps to better understand possible observations of $0\nu\beta\beta$-decay. Furthermore, such measurements also help in designing new detection techniques of solar neutrinos [14].

Accurate measurements of B(GT) values also help to understand nucleosynthesis for the elements heavier than iron. The most common models to describe nucleosynthesis are the s-, r-, p- and rp-processes [12]. These processes model the nucleosynthesis as long chains of neutron captures (s and r), proton captures (rp), or photo-dissociations (p), alternated by beta-decays. Hence, accurate knowledge of relevant B(GT) values is important to understand these processes.

Not only direct measurements of B(GT) values help to increase our understanding of nuclear structure, neutrino physics and nucleosynthesis, but also through comparison to theoretical models, lead to more confidence in the application of the models in regimes not accessible to experiments. Having theoretical models with good predictive power is important for being able to describe situations where direct measurements are (almost) impossible to perform [12]. Especially comparisons between experimental data and theoretical models that extend up to high excitation energy are useful, because this allows us to test the details of the theory. Such a comparison is made in Sect. 7 for a QRPA+QPVC model and for the data presented in this paper and indications for improving the model were obtained. However, other models (e.g., as described in Ref. [15]) may also benefit from such comparisons.

In the present work, the cross sections of the ^{116,122}Sn-(^{3}He, t)^{116,122}Sb charge-exchange reactions at 140 MeV/u were measured at very forward angles, including zero degrees. From these cross sections, the Gamow–Teller strength distributions were extracted for ^{116}Sb and ^{122}Sb between 0 and 28 MeV excitation energy. The experiment was performed using the high-energy resolution Grand Raiden spectrometer [16] at the Research Center for Nuclear Physics (RCNP) [17] at Osaka University in Osaka, Japan.

There exist two reasons for specifically investigating the ^{116,122}Sn $\rightarrow$ ^{116,122}Sb Gamow–Teller transitions. The first reason is that these isotopes provide important benchmarks for theoretical studies that can have implications on nucleosynthesis processes. The second reason is that when measuring the mentioned Gamow–Teller transitions by a (^{3}He, t) charge-exchange reaction, the spin-dipole (2^-) transitions can also be measured at the same time. ^{122}Sb has a 2^- g.s. and ^{116}Sb has a 2^- excited state at 518 keV [18], both of which are relatively strongly excited by a (^{3}He, t) charge-exchange reaction at 140 MeV/u. For $0\nu\beta\beta$-decay, the matrix elements of the spin-dipole transitions are also involved. Hence, it is important to find cases where such transitions occur (such as these), in order to gauge the theoretical calculations [19,20]. These spin-dipole transitions will be the subject of another paper, presenting the results of the data obtained in the same experimental campaign.

The level densities of the chosen Sb isotopes are quite high [18]. For this reason the Sn(^{3}He, t)Sb charge-exchange reaction was used, since it allows for good energy resolution in the measurements. This is possible because both the projectile and ejectile are charged particles and a magnetic spectrometer has been used for detection of the ejectile [21]. Because of this, the energy resolution was good enough to resolve the first few $\Delta L = 0, 1$ transitions. Finally, a beam energy of 140 MeV/u was chosen, because for this energy a systematic study was done for the reliability of extracting $B(GT)$ values from differential cross sections (which is about 5%) [21]. Earlier (^{3}He, t) measurements for Sn-targets (especially ^{116}Sn and ^{122}Sn) were performed at lower energies (e.g., at 67 MeV/u [22]). However, the extraction of $B(GT)$ values from cross sections at these lower energies is less reliable, since the spin–isospin term of the nucleon–nucleon interaction is not dominant at these energies.

In this paper, the measurement and data-analysis procedures will be discussed briefly in Sects. 2 and 3. Further details can be found in the PhD thesis of Ref. [23]. Subsequently, the measurement results (the B(GT) values) will be presented in Sect. 4. These results are then discussed by comparing them to other experiments [22,24] in Sects. 5 and 6

and to theoretical calculations in Sect. 7. Finally, an outlook is presented in Sect. 8 and our conclusions are summarised in Sect. 9.

2 Measurement procedure

The measurement was done using the high-resolution Grand Raiden spectrometer [16] at RCNP. A $^3He^{2+}$ beam of 140 MeV/u was produced with the coupled AVF and RING cyclotrons at RCNP [17,25] and then transported through the high-energy-resolution beam line called 'WS course' [26] to Grand Raiden. Using the 'WS course', the lateral and angular dispersion-matching techniques [27] were employed to obtain an energy resolution of $\sigma \approx 14$ keV (σ means that the resolution is expressed as a standard deviation). Contributions from differences in energy loss of tritons and ^{3}He in the target are not included in this number (see Sect. 3 for those contributions).

The used ^{116}Sn target had an areal density of 1.87 ± 0.01 mg/cm^2. For the ^{122}Sn target, it was 1.75 ± 0.01 mg/cm^2. Both targets were isotopically enriched above 95%. The ejected tritons were guided to the spectrometer focal plane in over-focus mode [28] to ensure a good sensitivity to the vertical scattering angle (this resolution was $\sigma_{\text{vert}} \approx 0.16°$). Thanks to the angular dispersion mode, sensitivity to the horizontal scattering angle was also guaranteed ($\sigma_{\text{hor}} \approx 0.1°$). Data were taken for two positions of Grand Raiden, i.e. for 0° and for 2.5°. In over-focus mode, the horizontal acceptance was roughly $\pm$ 1° around the designated position and the vertical acceptance was roughly $\pm$ 3° around zero.

Grand Raiden consists of two large dipole magnets for momentum separation and two quadrupole and higher-order magnets to focus the tritons and remove aberrations [16]. In the 0° position, the unreacted $^3He^{2+}$ beam was stopped in a Faraday cup inside the first dipole magnet. Due to the lateral dispersive mode, this Faraday cup did not have a perfect efficiency for stopping the beam [29]. In the 2.5° position, the $^3He^{2+}$ beam was stopped in a Faraday cup behind the first quadrupole magnet (with full efficiency). This setup is illustrated in Fig. 1.

The focal-plane detection system consists of two Multi-Wire Drift Chamber (MWDC) detectors and two plastic scintillators (10 mm thick) behind them, with a 10 mm thick aluminium plate between those scintillators to prevent that secondary electrons from one scintillator can produce a signal in the other. Both scintillators were equipped with a photomultiplier at each end. The trigger signal is a coincidence between the two scintillators (four photomultipliers). This signal provides a common start signal for the data taking. Each MWDC detector consists of two layers of alternating potential and sense wires. The first layer contains vertically oriented wires and the second one contains diagonally oriented wires. Hence, each MWDC detector is capable of providing two position coordinates of a passing triton track. With 4 such position coordinates in total, it is possible to reconstruct the horizontal and vertical positions and angle of incidence of the triton track at the focal plane.

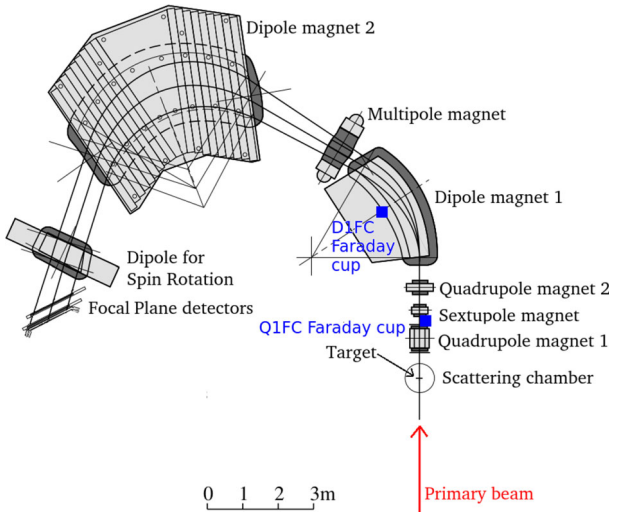

Fig. 1 Schematic overview of the Grand Raiden spectrometer; based on [25]

The data of the MWDC detectors and of the scintillators were first transported to a computer server and then saved on hard-disk memory without performing software operations of any kind. Subsequently, the data were converted offline to ROOT [30] format (version 5.34) using Gey's analyser code [31], which is a modified version of Tamii's analyser code [25] in the sense that it now generates output in the ROOT data format. All subsequent data analysis (see next section) was done using ROOT.

To calibrate the excitation energy and the horizontal and vertical scattering angles at the target, a sieve–slit measurement was performed. In such a measurement, a target with known, sharply defined, states (95% isotopically enriched ^{13}C for the present experiment) is used while a sieve slit (a multi-hole aperture) is placed between the target and the first magnet of the spectrometer (see Fig. 2). The sieve slit was given a regular rectangular pattern of small holes. The diameter of the holes was 2 mm, the horizontal spacing was 4 mm and the vertical spacing was 5 mm. The sieve slit was placed 585 mm downstream of the target. Since such a sieve slit cuts the scattered particle stream in a series of small pencil beams for which both the horizontal and vertical scattering angles at the target are known, the data of such a measurement allows us to determine the correspondence between the position and angle of incidence at the focal plane, and the horizontal and vertical scattering angles at the target. The computation of the correspondence is explained in the next section. When the states of the recoil nucleus are also well-known (for ^{13}C,

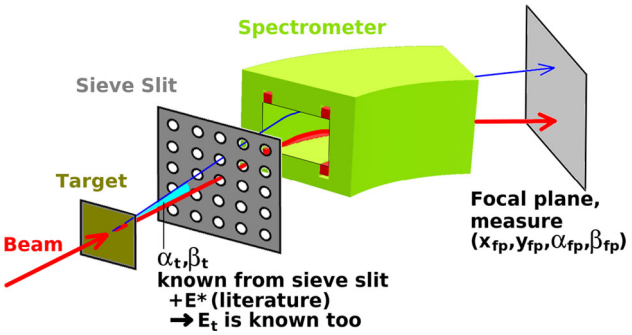

Fig. 2 Illustration of the sieve slit measurement used to calibrate the excitation energy and the horizontal and vertical scattering angles at the target

they can be found in Ref. [32]), this procedure can also be used to calibrate the excitation energy in a similar way.

3 Data analysis

Using the raw data from the MWDC detectors, the triton tracks passing through the focal plane were reconstructed, according to the procedure of Ref. [33]. The resulting lines were parameterised by $(x_{\mathrm{fp}}, y_{\mathrm{fp}}, \alpha_{\mathrm{fp}}, \beta_{\mathrm{fp}})$. x and y refer to the horizontal and vertical positions of the track intersecting the focal plane and α and β refer to the horizontal and vertical angles of incidence at that intersection. The subscript 'fp' refers to the focal plane.

Subsequently, the parameters $(x_{\mathrm{fp}}, y_{\mathrm{fp}}, \alpha_{\mathrm{fp}}, \beta_{\mathrm{fp}})$ were traced back to the target position event-by-event. The triton tracks at the target were parameterised by (E_t, α_t, β_t), where α_t and β_t are the horizontal and vertical scattering angles at the target and E_t is the kinetic energy of the ejected triton. The back-tracing procedure was applied by a mapping function $\boldsymbol{f}$ between the two sets of parameters. This mapping function was Taylor-expanded into (inverted) optical coefficients. Subsequently, these coefficients were fitted to the ^{13}C data using the sieve–slit calibration procedure described in the previous section (see Ref. [34] for more details). All coefficients up to third order were considered, along with the following higher-order terms: ${y_{\mathrm{fp}}}^4$, ${y_{\mathrm{fp}}}^4 x_{\mathrm{fp}}$, ${y_{\mathrm{fp}}}^4 {x_{\mathrm{fp}}}^2$, ${y_{\mathrm{fp}}}^5$, ${y_{\mathrm{fp}}}^6$, ${y_{\mathrm{fp}}}^2 {x_{\mathrm{fp}}}^2$ and ${x_{\mathrm{fp}}}^3 \theta_{\mathrm{fp}}$. Inspection of the ^{13}C data revealed that these specific higher-order coefficients had to be included to allow for an accurate fitting. However, because the sieve slit only had five holes in the horizontal direction, the data did not contain sufficient information to take other higher-order coefficients along in the fitting.

After the (inverted) optical coefficients were fitted to the ^{13}C data, the full scattering angle θ of the triton was reconstructed as $\theta^2 = {\alpha_t}^2 + {\beta_t}^2$, after shifting over the beam position, i.e. the 0°, obtained from the ^{3}He$^+$ peak and by using the approximation for small angles that $\tan(\theta) \approx \theta$. The excitation energy of the recoil nucleus was obtained through relativistic kinematics. Small ad hoc corrections were applied to the Sn data to correct for the higher-order aberrations that had to be neglected in the Taylor expansion. The Taylor expansion was found to break down above an excitation energy of 28 MeV. The excitation-energy spectra obtained in this way are shown in Figs. 3 and 4 for different ranges of the triton scattering angle θ.

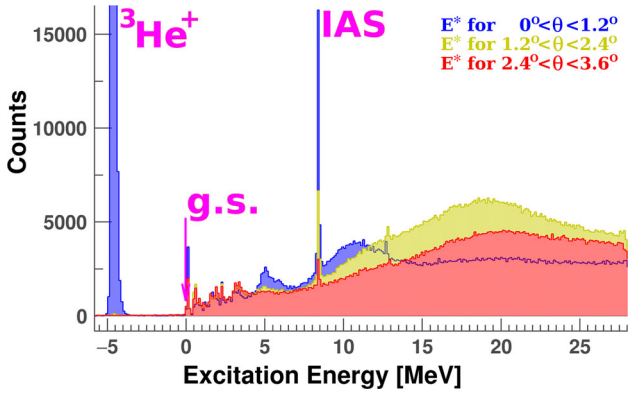

Fig. 3 Measured excitation-energy spectrum for the ^{116}Sn(^{3}He, t)^{116}Sb reaction for different ranges of the scattering angle θ at 140 MeV/u, obtained after a sieve–slit calibration

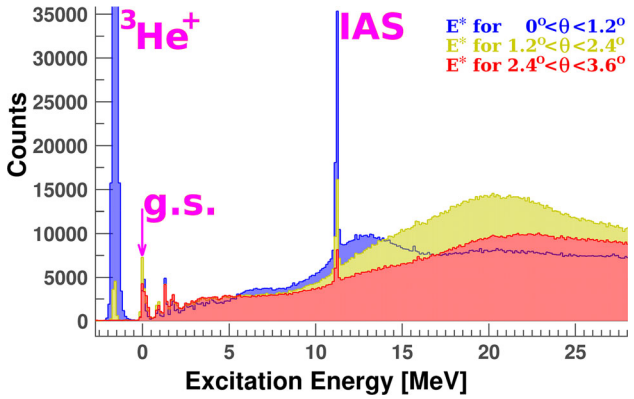

Fig. 4 Same as Fig. 3, but for the ^{122}Sn(^{3}He, t)^{122}Sb reaction

The differential cross sections for specific levels were extracted from the data using the following formula:

$$\frac{\mathrm{d}\sigma}{\mathrm{d}\Omega}(\theta) = \frac{P(\theta)}{\sum_n \epsilon_n(\theta) A_n(\theta) t_n Q_n}, \tag{2}$$

where n refers to a specific experimental run, θ refers to the polar scattering angle, t_n refers to the areal density of the target in number of particles per area, Q_n refers to the total number of beam particles in the experimental run (measured with the Faraday cups), A_n refers to the angular acceptance in sr, ϵ_n refers to the overall detection efficiency (wire chamber efficiency, dead time correction and analysis cuts) as a dimensionless number, and $P(\theta)$ refers to the total

number of counts measured for the level we are interested in (summed over all runs). This formula was derived from the definition of the differential cross section [35].

The data were divided into bins of 0.3° for the scattering angle θ. The angular acceptance was extracted from the data by plotting α_t versus β_t and defining a boundary where the number of counts drops. The detection efficiency ϵ was defined as the product of the efficiencies of the four MWDC layers, multiplied with $1-\tau$ where τ is the fraction of dead time of the DAQ. τ was measured individually for each experimental run and was of the order of 2%. The efficiency of an MWDC layer was defined as $N_4/(N_4+N_3)$, where N_4 is the number of events for which all four MWDC layers successfully detected a particle, and N_3 is the number of events where three MWDC layers successfully detected a particle [33]. By reconstructing triton tracks through the focal plane when only three MWDC layers produced a signal, and tracing these tracks back to the target using the optical coefficients, the numbers N_4 and N_3 could be determined specifically for each bin in θ and for each individual run. By artificially setting $\beta_{\rm fp}=0$, a track reconstruction through the focal plane became possible with only three MWDC layers. Due to the use of the over-focus mode, the information of $\beta_{\rm fp}$ is not crucial in subsequent analysis anyway. The detection efficiency per MWDC layer was found to be about 95% in the 0° mode and about 89% in the 2.5° mode.

$P(\theta)$ was determined from a Gaussian fit on top of a piecewise linear background for the peak corresponding to the level of interest. A separate Gaussian fit was made for each of the different bins in θ, but the counts from different runs were added to each other before the fit was made. Subsequently, the total number of counts in the fitted peak $P(\theta)$ was determined from the area under the Gaussian. Differential cross sections were also determined per excitation-energy bin of 200 keV by using the total number of measured counts in the bin as $P(\theta)$. A special procedure was applied to the so-called Isobaric Analogue State (IAS). The IAS is a Fermi resonance with an intrinsic width that is significantly smaller than the energy resolution for the present experiment [36]. It is, therefore, observed as a single peak in the excitation-energy spectrum. The IAS carries the full strength of the Non-Energy-Weighted Sum Rule (NEWSR) [1,37]. Just like the Gamow–Teller strength is specified in terms of B(GT) values, Fermi strength is specified in B(F) values. The definition of B(F) is identical to Eq. (1), except that the spin operator $\boldsymbol{\sigma}_j$ is not present in the equation. Since for (^{3}He, t) Fermi β^+ transitions are blocked in nuclei with $N>Z$, the Fermi NEWSR implies that for the IAS B(F) $=|N-Z|$, where N and Z are the numbers of neutrons and protons in the parent nucleus, respectively [1]. Since the IAS typically gives a very strong peak, the Gaussian fits were given exponentially decaying tails, so that good fits could be obtained despite the inaccuracies introduced by truncating our Taylor expansion in the sieve–slit calibration. For the other states, the number of counts was low enough so that normal Gaussian fits were sufficient for the present data analyses.

The IAS fits were also used to determine the energy resolution of the measurements, which was then applied to the fits of other states. These resolutions were phenomenologically determined to be $\sigma=\left(30.4+1.10\theta^2\right)$ keV for the ^{116}Sn target (θ is in degrees). For the ^{122}Sn target, an energy resolution of $\sigma=\left(32.6+1.25\theta^2\right)$ keV was obtained. These numbers are larger than the $\sigma\approx 14$ keV that was mentioned in the previous section. The difference is attributed to differences in energy loss of tritons and ^{3}He in the target, fluctuations in the magnetic field, and, the natural width of the IAS being the sum of its escape width and a spreading width due to coupling between the IAS and isovector giant monopole resonance (see Ref. [37] for more details).

In principle, the energy resolution of the measurements could also have been determined from a well-resolved low-lying state (below the proton and neutron emission thresholds). This is preferable, because unlike the IAS, those states below the particle emission threshold do not have a natural width due to particle emission. However, it turned out that for the data presented in this paper (see Figs. 3 and 4 and Ref. [18]) these low-lying states could not be individually resolved, due to the limited experimental energy resolution. Hence, for higher accuracy of the fits, it was decided to determine the experimental energy resolution from the IAS, which had much higher statistics. The energy resolution determined in this way turned out to be usable for accurate Gaussian fits of the low-lying states.

The $\Delta L=0$ components were extracted from the differential cross sections with a Multipole-Decomposition Analysis (MDA). The details of this procedure can be found in Ref. [24]. We performed an MDA based on contributions from different values of ΔL. Contributions up to $\Delta L=4$ were considered. For each ΔL contribution, only a single ΔJ contribution was considered in the MDA since contributions with the same ΔL but different ΔJ are very similar, so that any attempt to disentangle them would result in large systematic errors. For $\Delta L=0$, we considered $\Delta J=1$ (because we are interested in Gamow–Teller transitions). For $\Delta L=1$, we considered $\Delta J=2$ and for $\Delta L\geq 2$ we considered $\Delta J=\Delta L$ since those are usually the most dominant contributions. For the low-energy 1^+ states it is known beforehand that only the Gamow–Teller transition and the $\Delta L=2$, $\Delta S=1$, $\Delta J=1$ quadrupole transition can contribute. Hence, for such low-lying states only these two contributions were considered in the MDA.

The multipolarity contributions were computed with the code FOLD. The code FOLD was developed by Cook and Carr [38], based on the work of Petrovich and Stanley [39] and then modified as described in Refs. [40] and [41]. The One-Body Transition Densities (OBTDs) were computed in

Table 1 Optical-potential parameters used for the ^{116}Sn and ^{122}Sn targets

Nucleus	r_C [fm]	V_R [MeV]	r_R [fm]	a_R [fm]
^{116}Sn	1.25	33.11	1.354	0.836
^{122}Sn	1.25	33.45	1.349	0.839
Nucleus	V_I [MeV]	r_I [fm]	a_I [fm]	W_s [MeV]
^{116}Sn	45.88	1.016	1.147	12.0
^{122}Sn	46.14	1.017	1.155	12.0

the Normal Modes Formalism [37,42], using the code NORMOD [43,44]. For an overview of the theoretical formalism that is at the basis of the code FOLD, the interested reader is referred to Ref. [7]. For the optical potentials in the Distorted-Wave Born Approximation (DWBA), we assumed a Coulomb term, real and imaginary volume terms of the Woods–Saxon type, and an imaginary surface-Woods–Saxon term (with the same radius and diffuseness as the imaginary volume term), according to Ref. [45]. This procedure has already proven successful in Ref. [46] albeit without the surface term. The parameters were obtained from a linear interpolation of the parameters of the nuclei ^{12}C, ^{28}Si, ^{58}Ni, ^{90}Zr, and ^{208}Pb, obtained from Refs. [47,48]. The parameters of the outgoing channel were assumed equal to those of the incoming channel, except that the depths V_R, V_I and W_s were scaled by 0.85 [49]. The optical-potential parameters used for the present nuclei are listed in Table 1.

After the DWBA results of FOLD were obtained, they were smeared with $\sigma = 0.2°$ ($\sigma = 0.3°$) for the ^{116}Sn (^{122}Sn) target to take the vertical and horizontal angular resolutions into account as well as the binning in θ. The larger smearing for the ^{122}Sn target was due to a slight deterioration of the angular resolution of the beam. The smeared DWBA results of FOLD that form the basis of our MDA are illustrated in Figs. 5 and 6 for the ^{116}Sn target and excitation energies of zero and 20 MeV.

After the $\Delta L = 0$ component was extracted from the MDA fit of the differential cross sections, this component was extrapolated to zero momentum transfer $q = 0$ according to the procedure described in Ref. [3], which means that extrapolation is done by scaling the experimental $\theta = 0°$ result by the ratio of FOLD-computed results at $\theta = 0°$ and at $q = 0$, which properly takes the Q-value of the ground state and the excitation-energy dependence into consideration. Subsequently, B(GT) values were extracted using the following equations [3,21]:

$$\left.\frac{d\sigma}{d\Omega}\right|_{GT}^{(q=0)} = \hat{\sigma}_{GT} \cdot B(GT), \quad \hat{\sigma}_{GT} = K \cdot N^{D_{GT}} \cdot |J_{\sigma\tau}|^2, \quad (3)$$

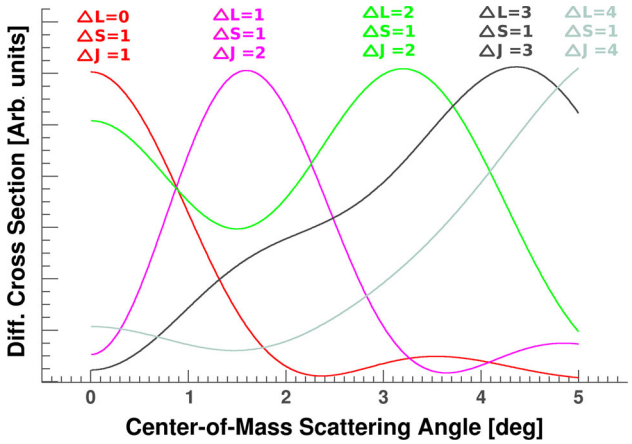

Fig. 5 Illustration of the different multipolarity components used in our MDA. The distributions were computed with FOLD and smeared with the detector resolution ($\sigma = 0.2°$ for the ^{116}Sn target and $\sigma = 0.3°$ for the ^{122}Sn target). The optical potentials of Table 1 were used. The specific distributions of this figure correspond to the ^{116}Sn target and an excitation energy of zero MeV and have been plotted such that the peaks have equal heights

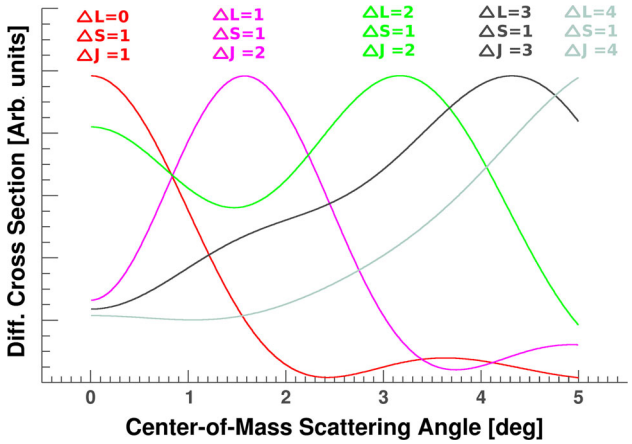

Fig. 6 Same as Fig. 5, but now for an excitation energy of 20 MeV

where K is a kinematic factor, $N^{D_{GT}}$ is the distortion factor given by the ratio of DWBA and PWBA (Plane-Wave Born Approximation) computed Gamow–Teller cross sections at $q = 0$ and $|J_{\sigma\tau}|$ is the volume integral of the central $\sigma\tau$-component of the effective nucleon–nucleon interaction between the projectile and target nucleons [1,3]. The product of these three quantities is the so-called unit cross section. A similar equation also applies for Fermi cross sections, however, $|J_{\sigma\tau}|$ should then be replaced by $|J_\tau|$, the volume integral of the central τ-component, and $N^{D_{GT}}$ by N^{D_F}, the distortion factor for Fermi transitions. The Fermi and Gamow–Teller unit cross sections at 140 MeV/u can, with an uncertainty of 5%, be phenomenologically described by [21]

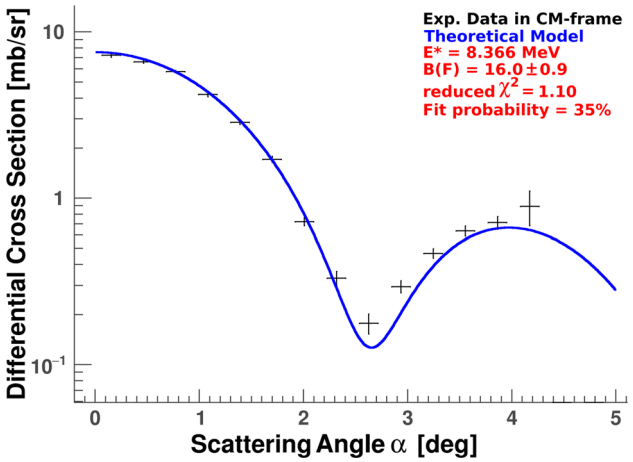

Fig. 7 Extracted differential cross section of the IAS for the ^{116}Sn(^{3}He, t)^{116}Sb reaction at 140 MeV/u. The theoretical model is computed with FOLD as described in the text, and fitted to the data with the overall normalisation as the only variable parameter. The fit probability is the area under the reduced χ^2 distribution to the right of the reduced χ^2 value of the fit

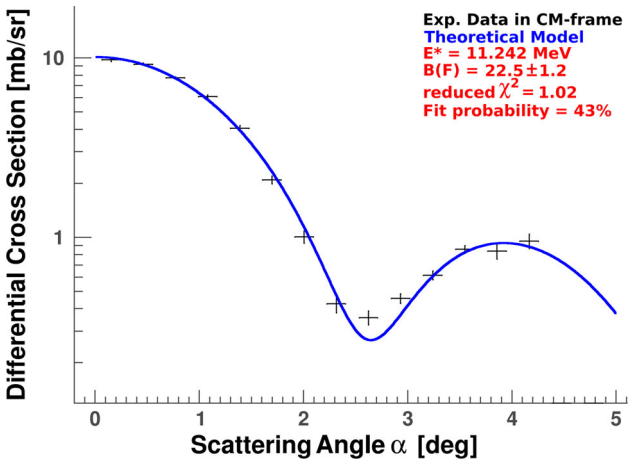

Fig. 8 Same as Fig. 7, but now for the ^{122}Sn(^{3}He, t)^{122}Sb reaction

$$\hat{\sigma}_{\mathrm{GT}} = A^{-0.65} \cdot 109 \text{ mb/sr}, \qquad \hat{\sigma}_F = A^{-1.06} \cdot 72 \text{ mb/sr}. \tag{4}$$

The use of Eqs. (3) and (4) and Table 1 was first tested on the IAS for both targets. The IAS presents an excellent benchmark for this, since for this state B(F) = $|N - Z|$. The results are shown in Figs. 7 and 8. In these figures, the reduced χ^2 value (red. χ^2) and the probability of the fit are also shown. The fit probability is the area under the reduced χ^2 distribution to the right of the red. χ^2 value of the fit.

For the runs taken at 0° and 2.5°, different Faraday cups were used to integrate the charge deposited by the beam (see Fig. 1: D1FC was used for 0° and Q1FC was used for 2.5°). By comparing the angular distributions in the range in which the 0° and 2.5° settings overlap ($1.5° \leq \theta \leq 3.3°$), it was found that the cross sections differed by 16%. Based on Ref. [29], in which a similar discrepancy was encountered and diagnosed as being due to incomplete charge integration for the 0° setting, the cross sections for the 0° setting were reduced by 16%.

The angular distributions of the IAS were used to fine-tune the optical-potential parameter W_s used in the DWBA calculations to reduce the uncertainty in the MDA procedure. It was found that by including an imaginary surface Woods–Saxon potential, the location of the first minimum in the experimental angular distribution could be better reproduced by the calculation. Therefore, this surface Woods–Saxon potential was included for all DWBA calculations. Based on the IAS distributions, W_s was determined to be 12 MeV. W_s was the only parameter of Table 1 that was fine-tuned in the DWBA from the original value of zero [46] to 12 MeV.

The above data-analysis procedure resulted in B(F) = 16.0 ± 0.9 for the ^{116}Sn target and in B(F)= 22.5 ± 1.2 for the ^{122}Sn target. Since these are in good agreement with the expected B(F) = $|N - Z|$, and the red. χ^2 values are close to unity, we conclude that our analysis procedure can be used to reliably extract B(GT) values.

4 Results

The B(GT) values for the low-lying states were extracted from the differential cross sections of observed discrete states. Since both target nuclei have a 0^+ ground state, any $0^+ \rightarrow 1^+$ transition in our excitation-energy region is only possible through a Gamow–Teller or a quadrupole ($\Delta L = 2$, $\Delta S = 1$, $\Delta J = 1$) excitation. Therefore, as discussed in the previous section, these contributions were the only two contributions considered in the MDA. All low-lying states in the excitation-energy spectrum that could be resolved, were considered. The corresponding peaks are illustrated in Figs. 9 and 10. If the differential cross section versus scattering angle of the state showed a 1^+ character (illustrated in Figs. 11 and 12 for the states labelled 1), the B(GT) value of the state was reported in Tables 2 and 3, together with the measured mean excitation energy (Meas. E^*), the Number of Degrees of Freedom (NDF) and the reduced χ^2 value of the MDA fit (red. χ^2). The NDF is different for different states, because for weaker states it was not always possible to obtain accurate Gaussian fits for some of the angular bins. These bins and the corresponding datapoints were omitted in the MDA fit, causing the NDF to vary slightly. For some states, the measured mean excitation energy could also be matched to the NNDC database [18]. In the situations where this matching was possible, the 1^+ character of the state was confirmed and the corresponding excitation energy from ref. [18] was also shown (Lit. E^*). The measurement errors of the B(GT)

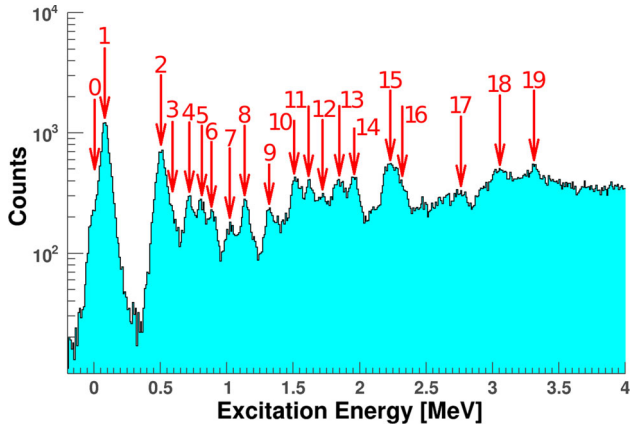

Fig. 9 States that could be resolved in the low-energy region of the excitation-energy spectrum for the ^{116}Sn(^{3}He, t)^{116}Sb reaction

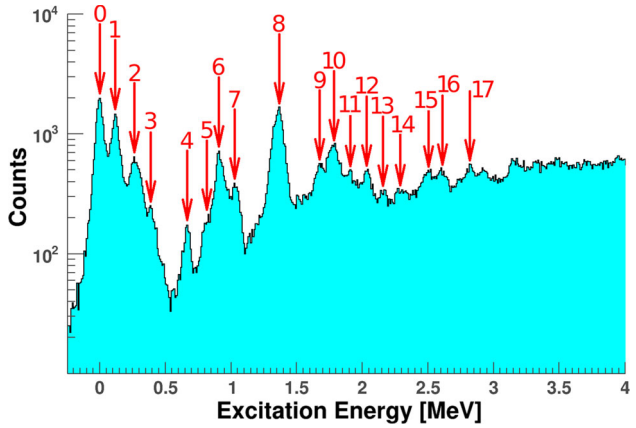

Fig. 10 Same as Fig. 9, but now for the ^{122}Sn(^{3}He, t)^{122}Sb reaction

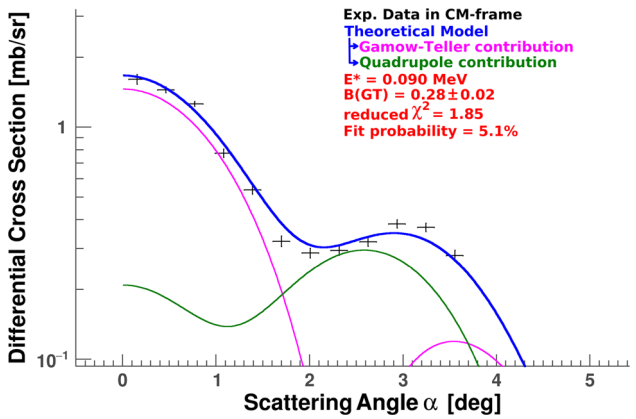

Fig. 11 Angular distribution of the differential cross section and the performed MDA of the state labelled 1 in Fig. 9

values contain a statistical contribution, a 1% contribution from the extrapolation to $q = 0$ and a 5% contribution from the uncertainty of Eq. (4).

To study the Gamow–Teller transitions at higher excitation energies, the differential cross section was extracted per

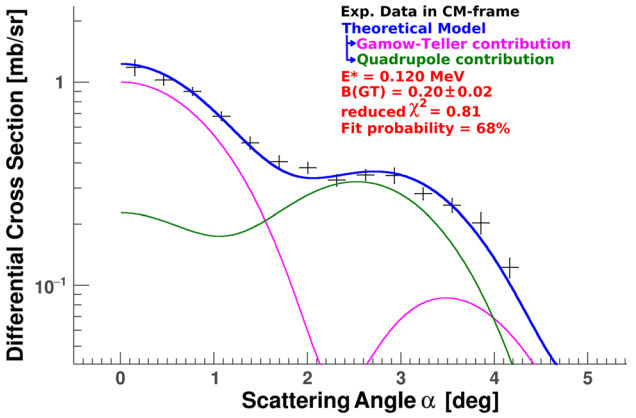

Fig. 12 Same as Fig. 11, but now for the state labelled 1 in Fig. 10

bin of 200 keV. In this situation, the MDA as described in the previous section (with all contributions up to $\Delta L = 4$) was used to extract the $\Delta L = 0$ contribution. The resulting Gamow–Teller strength distributions are shown in Figs. 13 and 14. The systematic error from the MDA is shown as a grey band in Figs. 13 and 14 and has been estimated by fitting the differential cross sections without the $\Delta L = 4$ contribution in the MDA.

The Gamow–Teller strength distributions were obtained for two different situations. In the first case, the distributions were extracted without subtracting the quasi-free background, meaning that the full $\Delta L = 0$ contribution to the differential cross section at 0° was used as input to Eq. (3) after extrapolation to $q = 0$. This procedure is similar to that of Ref. [24]. The different multipolarity contributions to the differential cross section at 0° are illustrated for this situation in Figs. 15 and 16.

In the second case, the quasi-free background [22,37] was subtracted before the MDA was performed. To subtract the quasi-free background, the quasi-free differential cross section was subtracted from the differential cross section per bin of 200 keV (which was determined from the measured number of counts in that bin). To compute the quasi-free differential cross section, the model from Ref. [22] was used:

$$\frac{\mathrm{d}^2\sigma}{\mathrm{d}\Omega dE^*}(E^*,\theta) = N_0 \cdot \frac{1 - e^{(E_t - E_0)/T}}{1 + ((E_t - E_{QF})/W)^2}, \qquad (5)$$

where E_t is the kinetic energy of the ejected triton, which depends on θ and on the excitation energy E^*. The other quantities are model parameters. Equation (5) applies only in the situation where $E^* > S_p$ (the quasi-free background is zero otherwise [22,37]). In our analysis, T and W were fixed to the same values used in Refs. [22,50]: $T = 100$ MeV and $W = 22$ MeV. W accounts for the Fermi momentum of the neutron in the target nucleus that is transferred and T has the characteristics of a temperature. In Ref. [50], searches for the

Table 2 B(GT) values for the states at low excitation energy obtained from the ^{116}Sn(^{3}He, t)^{116}Sb reaction at 140 MeV/u. The Lit. E^* values were taken from Ref. [18], while the Meas. E^* values come from the data presented in this paper. For the labelling of the states, see Fig. 9

Nr.	Meas. E^* [MeV]	Lit. E^* [MeV]	red. χ^2	NDF	$B(GT)$
1	0.090	0.094	1.83	10	0.28 ± 0.02
4	0.713	0.732	5.67	9	0.051 ± 0.005
6	0.905	0.918	2.89	10	0.035 ± 0.004
8	1.146	1.158	1.25	11	0.049 ± 0.005
9	1.338	1.386	2.85	10	0.034 ± 0.004
10	1.525	–	3.24	9	0.028 ± 0.003
11	1.613	–	4.20	8	0.031 ± 0.004
13	1.841	–	2.26	9	0.022 ± 0.003
14	1.956	–	2.72	11	0.038 ± 0.004
15	2.219	–	3.66	8	0.062 ± 0.005
16	2.292	–	1.58	8	0.072 ± 0.006
17	2.739	–	1.73	7	0.027 ± 0.003
18	3.065	–	1.77	12	0.008 ± 0.003
19	3.318	–	1.68	11	0.013 ± 0.003

Table 3 Same as Table 2, but now for the ^{122}Sn(^{3}He, t)^{122}Sb reaction. For the labelling of the states, see Fig. 10

Nr.	Meas. E^* [MeV]	Lit. E^* [MeV]	red. χ^2	NDF	$B(GT)$
1	0.120	0.122	0.81	12	0.20 ± 0.02
4	0.667	0.620	0.72	7	0.023 ± 0.002
8	1.358	–	2.32	12	0.22 ± 0.02
9	1.675	–	1.45	11	0.026 ± 0.003
10	1.780	–	3.70	12	0.059 ± 0.005
12	2.030	–	4.41	12	0.021 ± 0.003
13	2.172	–	1.48	11	0.012 ± 0.002
14	2.312	–	2.05	10	0.018 ± 0.003
15	2.499	–	2.27	12	0.035 ± 0.003
16	2.597	–	1.62	10	0.025 ± 0.003
17	2.845	–	1.02	12	0.026 ± 0.003

values of W and T were performed. The obtained values for W are about the same for (^{3}He, t) for all studied target nuclei as well as for pion-exchange, namely 22 MeV. Furthermore, in Ref. [50], only a weak temperature dependence was found.

According to Ref. [22], the parameter E_0 was modelled as $E_0 = E_t(E^* = 0) - S_p$, where S_p is the proton-separation energy of the recoil nucleus. This leaves the parameters N_0 and E_{QF} to be fitted to the data. By varying E_{QF}, it was confirmed that the shape produced by the model in Eq. (5) is not very sensitive to the precise value of E_{QF}. However, the value given in Ref. [22] ($E_{QF} = 180$ MeV) should be adapted to a beam energy of 140 MeV/u, which is why we did refit the parameter E_{QF}.

On the other hand, the choice of N_0 is very important, because it determines the overall normalisation and, therefore, the total amount of quasi-free background. Unfortunately, it is difficult to accurately determine N_0 due to a lack of knowledge of the quasi-free background [37]. Therefore, we chose to check two extremes. The first one being $N_0 = 0$, which corresponds to no subtraction of quasi-free background. The other one is where the quasi-free background is as large as possible, and this scenario will be denoted as N_0 being maximal. In this scenario, we assume that all contributions to the total differential cross section above the IV(S)GDR come from the quasi-free background. This scenario corresponds to what was used in Ref. [22] (see Fig. 17 for an illustration). However, as the IV(S)GDR is very broad, this does not necessarily mean that at 28 MeV, the total differential cross section consists of only quasi-free background. Moreover, the analysis procedure used in Ref. [22] assumes that in addition to the IAS, there is only the Gamow–Teller Resonance (GTR), pygme resonances, the IV(S)GDR and the quasi-free background, which is a simplification of reality. As a result, it is still possible that after subtracting the quasi-free background, a proper MDA analysis reveals a small $\Delta L = 0$ contribution at high excitation energies, possibly corresponding to the low-energy tail of the IV(S)GMR [36]. With the assumption of N_0 being maximal, Eq. (5) can

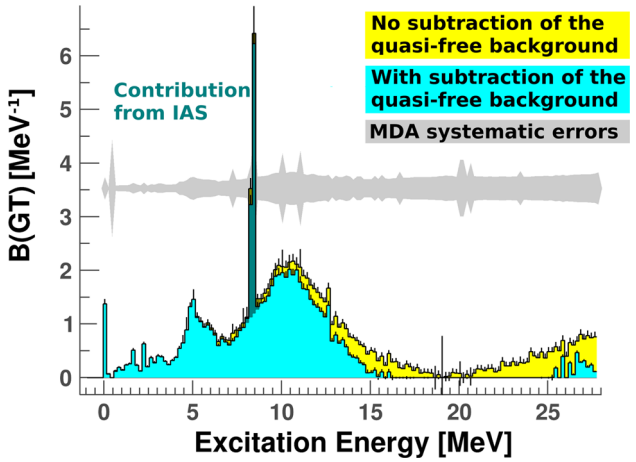

Fig. 13 B(GT) spectrum for the ^{116}Sn(^{3}He, t)^{116}Sb reaction at 140 MeV/u. Both the situation where the quasi-free background is not subtracted and the situation where the upper bound of the quasi-free background is subtracted are shown. Note that if the subtraction leads to negative B(GT) values, they are set to zero in the figure

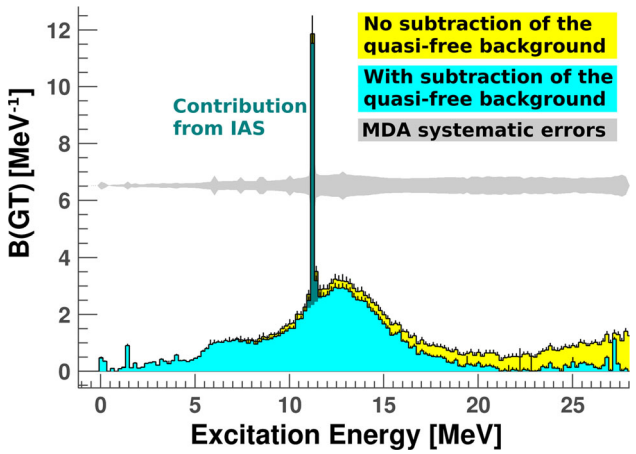

Fig. 14 Same as Fig. 13, but now for the ^{122}Sn(^{3}He, t)^{122}Sb reaction

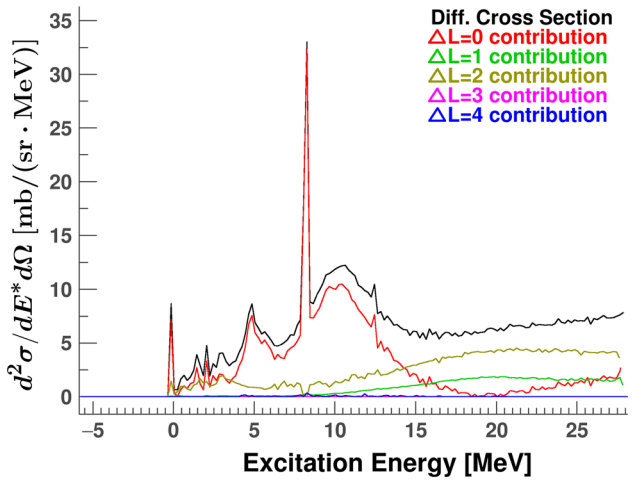

Fig. 15 Different multipolarity contributions to the differential cross section for the ^{116}Sn(^{3}He, t)^{116}Sb reaction at 140 MeV/u without subtraction of the quasi-free background. The $\Delta L = 3$ and $\Delta L = 4$ contributions are relatively small

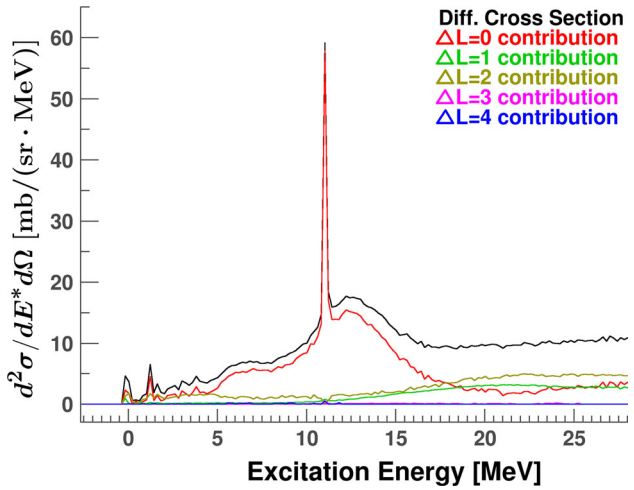

Fig. 16 Same as Fig. 15, but now for the ^{122}Sn(^{3}He, t)^{122}Sb reaction at 140 MeV/u

be fitted to the data and this situation corresponds to the largest possible quasi-free background contribution.

It is not a common procedure to subtract the quasi-free background before applying MDA. The reason for this is that the use of equation (5) can bias the MDA procedure. For example, an overestimation of N_0 might result in an underestimation of Gamow–Teller strength. This will be discussed in more detail in Sect. 6. However, not subtracting any quasi-free background could lead to an overestimation of the Gamow–Teller strength. Since the correct quasi-free contribution is very difficult to determine [37], we decided to apply both strategies ($N_0 = 0$ and N_0 being maximal as discussed above), so that it is known for sure that the true Gamow–Teller distribution is between the two distributions presented in Figs. 13 and 14. Another reason for pursuing both strategies is that we wanted to be able to compare our results to those published in Ref. [22] (where putting N_0 to its maximal value was chosen) and to those published in Ref. [24] (where putting $N_0 = 0$ was chosen). These comparisons are discussed in the next two sections.

We further note that, since the IAS is identified as a $\Delta L = 0$ contribution in the MDA, it shows up in the B(GT) distributions of Figs. 13, 14, 15 and 16. However, its contribution is, of course, removed before further discussing Gamow–Teller strength in the data.

As a final remark, it is noted that the extraction of Gamow–Teller strength from a charge-exchange reaction always contains an additional systematic uncertainty due to interference between the $\Delta L = 0$ and $\Delta L = 2$ amplitudes for $\Delta J = 1$ excitations. This interference is mediated by the tensor-τ component of the nucleon–nucleon interaction and cannot be removed through the MDA analysis. It has been shown

[51,52] that, for the (^{3}He, t) reaction, $B(GT)$ measurements deviate from the true value. These deviations are relatively stronger for weak Gamow–Teller transitions, and they are, on average, zero. The magnitude for this systematic uncertainty could be estimated on a state-by-state basis by the following relationship (see Eq. (6) and Fig. 6 in Ref. [51] and Eq. (4) and Fig. 4 in Ref. [52]):

$$\frac{\Delta \mathrm{B(GT)_{tensor}}}{\mathrm{B(GT)}} \approx 0.03-0.035 \cdot \ln(\mathrm{B(GT)}), \quad (6)$$

where $\Delta \mathrm{B(GT)_{tensor}}$ denotes the absolute systematic uncertainty due to the interference described above. The systematic uncertainty from Eq. (6) was not shown in Tables 2 and 3 and also not in Figs. 13 and 14, because it only becomes significant for (very) small B(GT) values due to the logarithmic behaviour. For this reason, it should be noted that the Gamow–Teller ($\Delta L = 0$) cross section gets very small in the excitation-energy region of 16−28 MeV for the ^{116}Sn target. It is much smaller than the ones for the major $\Delta L = 1$ and $\Delta L = 2$ components. Thus, extraction of the small $\Delta L = 0$ component is difficult in this region, and leads to a large uncertainty in the $\Delta L = 0$ cross section. The uncertainty in the extraction of the Gamow–Teller strength is, therefore, increased due to the tensor effect described above and other effects.

To further investigate the reliability of the measurements presented in this paper and to explore the uncertainty in N_0 of the quasi-free background, we will compare the measurements presented in this paper to the results presented in Refs. [22] (Pham et al.) and [24] (Guess et al.) in the next sections.

5 Comparison to the results presented in Ref. [22]

Pham et al. [22] studied the Gamow–Teller strength distributions in the Sn(^{3}He, t)Sb reaction for several isotopes (among them are the two isotopes discussed in this work), but for a beam energy of 67 MeV/u. We have compared the data presented in this paper to theirs for the ^{116}Sn and ^{122}Sn targets. Pham et al. studied the Gamow–Teller distribution by fitting the excitation-energy spectrum to a sum of Gaussians. Five Gaussians (labelled GT1-GT5) were used to fit the Gamow–Teller (GT) resonances: the GTR [36] and the pygmy resonances [22]. A sixth Gaussian was used to fit the IAS and a seventh was used to fit the isovector (spin) giant dipole resonance (IV(S)GDR) [36]. The quasi-free background model of Eq. (5) was also added. This procedure is illustrated in Fig. 17 for the data presented in this paper. For this figure, it should be noted that, technically, Pham et al. applied a condition of $-0.3° \leq \alpha_t \leq 1.3°$ to their data, while we applied $0° \leq \theta \leq 1.3°$ to the present data (see Fig. 17 and note that $\theta^2 = {\alpha_t}^2 + {\beta_t}^2$). Since the vertical acceptance (β_t) of the spectrometer used by Pham et al. was only $\pm 0.5°$, the scattering angle could be approximated by $\theta \approx |\alpha_t|$ and a condition on α_t alone was sufficient. However, the vertical acceptance (β_t) of the present experiment is of the order of $\pm 3°$, which makes it necessary to use the full scattering angle θ in the condition for the data presented in this paper.

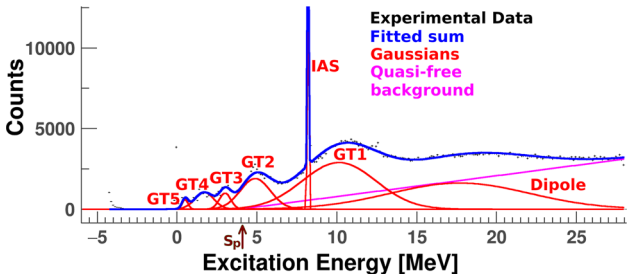

Fig. 17 Illustration of the fitting procedure used by Pham et al. [22], applied to the present ^{116}Sn data and subjected to the condition $0° \leq \theta \leq 1.3°$

Pham et al. reported the Gamow–Teller cross sections as determined from the Gaussian fits illustrated in Fig. 17. The data in the range of $-0.3° \leq \alpha_t \leq 1.3°$ were used for these fits and the $\Delta L \neq 0$ multipolarity contributions were not subtracted. However, B(GT) values were not extracted from these cross sections. Hence, we have taken the cross sections reported by Pham et al., corrected them for the smearing effects of $-0.3° \leq \alpha_t \leq 1.3°$ and extrapolated them to $q = 0$. This was done using the code FOLD introduced in Sect. 3 and the optical potentials from Ref. [45]. These potentials are different from Table 1 because of the difference in beam energy.

Subsequently, the B(GT) values were extracted using Eq. (3). To determine the Gamow–Teller unit cross section at 67 MeV/u, a two-point MDA was performed on the data published in Ref. [22]. For ^{118}Sb, Ref. [22] provided the differential cross section under the condition $-0.3° \leq \alpha_t \leq 1.3°$ and under the condition $1.3° \leq \alpha_t \leq 2.9°$ (see Fig. 2 in that paper). These results provided two data points like the ones in Figs. 11 and 12. With two data points only, an MDA can at most distinguish two multipolarity contributions (hence, a two-point MDA). We chose a $\Delta L = 0$ contribution (The Gamow–Teller one) and a $\Delta L = 2$ contribution, which are the same two contributions used to calculate the numbers in Tables 2 and 3. With this two-point MDA, the Gamow–Teller multipolarity contribution to the ^{118}Sb ground state cross section was determined to be $(87 \pm 9)\%$.

Since for all other isotopes, Ref. [22] only provided differential cross sections under the condition $-0.3° \leq \alpha_t \leq 1.3°$, ^{118}Sb was the only isotope for which the Gamow–Teller contribution to the ground state could be established at 67 MeV/u. For this reason, we chose to first determine the unit cross section for the ^{118}Sn target, and then to extrapolate this result to the isotopes of interest. For this extrapolation,

Table 4 Comparison between B(GT) values (B(F) for the IAS) for the ^{116}Sn(^{3}He, t)^{116}Sb reaction obtained from the present experiment and those obtained from fitting Pham et al., data. See text for details

State	Ref. [22] 67 MeV/u	Gaussians 140 MeV/u	Spectrum 140 MeV/u
IAS	16	17.9 ± 0.9	16.0 ± 0.9
GT1	9.5 ± 2.2	13.7 ± 0.7	9.82 ± 0.51
GT2	3.0 ± 0.7	3.4 ± 0.5	2.39 ± 0.14
GT3	1.0 ± 0.3	0.7 ± 0.1	0.10 ± 0.04
GT4	1.2 ± 0.3	1.2 ± 0.3	0.83 ± 0.09
GT5	0.3 ± 0.1	0.2 ± 0.2	0.50 ± 0.20
Σ(B(GT))	15.0 ± 3.3	19.2 ± 1.1	13.81 ± 0.79

Table 5 Same as Table 4, but now for the ^{122}Sn(^{3}He, t)^{122}Sb reaction

State	Ref. [22] 67 MeV/u	Gaussians 140 MeV/u	Spectrum 140 MeV/u
IAS	22	28.6 ± 1.5	22.5 ± 1.2
GT1	12.8 ± 3.0	23.0 ± 1.2	17.06 ± 0.87
GT2	4.6 ± 1.1	5.5 ± 0.6	3.14 ± 0.19
GT3	3.2 ± 0.8	3.0 ± 0.3	1.00 ± 0.16
GT4	0.6 ± 0.2	0.2 ± 0.1	0.04 ± 0.03
GT5	–	0.3 ± 0.1	0.5 ± 0.7
Σ(B(GT))	21.2 ± 4.6	31.9 ± 1.7	23.18 ± 1.31

theoretical estimates of K, N^D and $|J_{\sigma\tau}|$ (see Eq. (3)) were used, so that the ratio of theoretical unit cross sections for the ^{116}Sn and ^{118}Sn targets could be computed. This ratio was then multiplied with the ^{118}Sn unit cross section determined from the two-point MDA. We found a Gamow–Teller unit cross section of 2.53 mb/sr for the ^{116}Sn target at 67 MeV/u. For the ^{122}Sn target, a similar procedure was used and we found a Gamow–Teller unit cross section of 2.40 mb/sr. The inaccuracies of the two-point MDA and of the ^{118}Sb data from ref. [22] cause the above cross sections to contain an uncertainty of 20% (which is a correlated error between the ^{116}Sn and ^{122}Sn targets).

The comparisons between the B(GT) values obtained from the Pham et al. data and the B(GT) values obtained from the present experiment are shown in Tables 4 and 5.

The first columns in Tables 4 and 5 show the labelling of the states according to Fig. 17. The second columns show the $B(GT)$ values obtained from the cross sections reported by Pham et al. (B(F) is obtained from the Fermi NEWSR). The third columns show the B(GT) values obtained from the present experiment, but analysed according to the procedures of Pham et al. (Gaussian fits of the excitation-energy spectrum like in Fig. 17, i.e. no MDA and a single angular bin of $0° \leq \theta \leq 1.3°$). The fourth columns are obtained from fitting Gaussians like in Fig. 17 not to the excitation-energy spectrum, but to the Gamow–Teller distributions in Figs. 13 and 14 (the case where the quasi-free background is subtracted, since that is what was done in Ref. [22]). The IAS values in these columns were obtained from Figs. 7 and 8. This essentially means that the difference between the third and fourth columns is the elimination of the $\Delta L \neq 0$ multipolarity contributions. For the third and fourth columns, the unit cross sections of Eq. (4) were used. For the second column, the derived unit cross sections (discussed above) at 67 MeV/u were used.

Obviously, a fair comparison to Pham et al., requires the use of the same analysis procedures. Hence, a comparison should only be made between the second and third columns of Tables 4 and 5. In these two columns, there is only a significant deviation between the present data and those of Pham et al. for the IAS and GT1 of the ^{122}Sn target. The deviation in the IAS is easily explained, as Pham et al., simply assumed B(F) $=|N - Z|$ for the IAS. The number in the third column, on the other hand, was obtained from a pure Gaussian fit (see Fig. 17). However, in Sect. 3 it was already discussed that a pure Gaussian was not suitable for fitting the IAS and that exponential tails had to be included. This inclusion is reflected in the numbers presented in the fourth columns. Hence, the fourth columns should show the correct numbers. The deviation in GT1 could be a result of systematic uncertainties in the fitting procedure of Fig. 17. The present data show that the excitation-energy spectrum of the ^{122}Sn target is almost flat between GT1 and GT2 (see Fig. 4), while that of the ^{116}Sn target shows a clear dip (around 6 MeV; see Fig. 3). Hence, fitting Gaussians to GT1 and GT2 may result in a significant systematic uncertainty for GT1 for the ^{122}Sn target. These systematic uncertainties were not included in Tables 4 and 5 because due to the flatness of the excitation-energy spectra, they could not be accurately determined. This could explain the GT1 discrepancy. The data in the figures shown in Pham et al. [22] do not disagree with this explanation.

Pham et al., also reported cross sections for the individual low-lying Gamow–Teller states. B(GT) values could be extracted from these cross sections in a similar way as was done for the states GT1–GT5 in Tables 4 and 5, but the B(GT) values obtained from the Pham et al., cross sections are much higher than those presented in Tables 2 and 3. The reason for this, is that Pham et al., did not include the description of a piecewise linear background in the determination of the cross sections (like we did). This background is significant for all states in Tables 2 and 3, except for the first ones. For those states, the cross sections of Pham et al. provided us with B(GT)= 0.39 ± 0.09 for the first Gamow–Teller state of the ^{116}Sn target. For the first Gamow–Teller state of the ^{122}Sn target, this was B(GT)= 0.33 ± 0.07. The differences between these values and those in Tables 2 and 3 are not too big, but also not insignificant. To obtain these two B(GT) values from fitting the data of Pham et al., we assumed that the Gamow–Teller contribution to the cross section was 87%.

This assumption came from the two-point MDA we used to obtain the Gamow–Teller unit cross section for the ^{118}Sn target at 67 MeV/u (see discussion above). There, it was established that the Gamow–Teller contribution to the total cross section was $(87 \pm 9)\%$. However, this number contains a large uncertainty and secondly, there is no a priori reason to assume that this number is the same for the first Gamow–Teller states of the ^{116}Sn and ^{122}Sn targets (Ref. [22] does not contain the required data to obtain these numbers for the ^{116}Sn and ^{122}Sn targets). If the Gamow–Teller contribution would be somewhat lower than 87%, the discrepancies would disappear.

Finally, there is the issue that Pham et al., claim that GT1 contains $(65 \pm 3)\%$ of the Ikeda sum rule for all isotopes investigated. However, the second columns of Tables 4 and 5 claim that GT1 of the ^{116}Sn target, as it was determined from the cross sections presented in Pham et al., only contains $(14 \pm 3)\%$ of the Ikeda sum rule. For the ^{122}Sn target, this is $(19 \pm 5)\%$. The percentage of $(65 \pm 3)\%$ from Pham et al., was computed with the following equation [22,36,53,54]:

$$\mathrm{B(GT)} = \frac{\sigma_{\mathrm{GT}}}{\sigma_{\mathrm{IAS}}} \cdot \frac{k_{\mathrm{f}}^{\mathrm{IAS}}}{k_{\mathrm{f}}^{\mathrm{GT}}} \cdot \frac{|N-Z|}{D}, \; D = \frac{\hat{\sigma}_{\mathrm{GT}}}{\hat{\sigma}_{\mathrm{F}}}, \tag{7}$$

where σ_{GT} is the measured Gamow–Teller cross section, σ_{IAS} is the measured IAS cross section (which was reported in Ref. [22]), $k_{\mathrm{f}}^{\mathrm{IAS}}/k_{\mathrm{f}}^{GT}$ is the ratio of the wave numbers of the outgoing ejectile (usually around unity) and D is the ratio of Fermi and Gamow–Teller unit cross sections. Pham et al., applied Eq. (7) with $D = (E/E_0)^2 = 1.48$ ($E_0 = 55.0 \pm 0.4$ MeV) [54]. However, $D = (E/E_0)^2 = 1.48$ only applies to (p, n) reactions, while Pham et al., used the $(^3\mathrm{He}, t)$ reaction. With the IAS cross sections from Pham et al. (which carry an uncertainty of 10% [50]) and our derived Gamow–Teller unit cross sections at 67 MeV/u (which carry an uncertainty of 20% as discussed above), we find $D = 5.2 \pm 1.1$ for $(^3\mathrm{He}, t)$ at 67 MeV/u. This explains the large difference. Taking this into consideration, our results are in reasonable agreement with the data presented in Ref. [22] if we follow the same analysis procedure. This confirms the reliability of our measurements.

6 Comparison to the results presented in Ref. [24]

We chose to include a comparison between the present data and the Gamow–Teller strength distribution of the ^{150}Nd(^{3}He, t)^{150}Pm reaction studied by Guess et al. [24] at 140 MeV/u to further validate our data analysis and to explore the issue of whether the quasi-free background should be subtracted or not (see Sect. 4). Even though a completely different target nucleus was studied, the experiment of Guess et al., is particularly suited for this purpose,

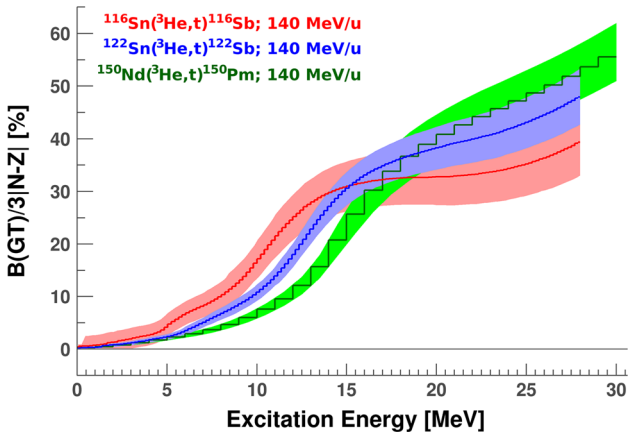

Fig. 18 Full integral of the B(GT) spectra as a function of the excitation energy up to where the integral was truncated. The data on ^{150}Nd(^{3}He, t)^{150}Pm were obtained from Guess et al. [24]. The other data were obtained from Figs. 13 and 14. Systematic errors from the MDA fitting procedure were included in the error bands

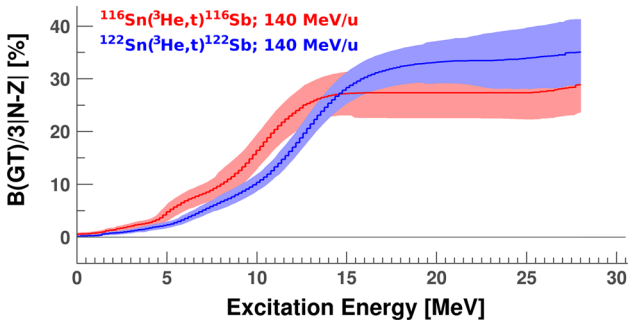

Fig. 19 Same as Fig. 18, except now the quasi-free background was subtracted (with N_0 being maximal). The ^{150}Nd(^{3}He, t)^{150}Pm results are not shown for this situation, since those data were not available in Ref. [24]

because the experimental setup, the beam energy and the data-analysis procedures followed are completely identical to ours. The only difference is that Guess et al., did not subtract the quasi-free background, implying that their analysis procedure corresponds to our $N_0 = 0$ scenario introduced in Sect. 4.

We have chosen to make the comparison by plotting the integral of the Gamow–Teller distributions between 0 and a certain excitation energy versus that excitation energy. This way, implications for the general quenching phenomenon of the Gamow–Teller resonance can be easily visualised. The plots are shown in Fig. 18. The data from Guess et al., include the systematic error contribution from the MDA. Hence, for the present data we have chosen to include this contribution as well. For completeness, the results with the quasi-free background subtracted (with N_0 being maximal) are shown in Fig. 19 for the present data. Corresponding results (N_0 being maximal) concerning the ^{150}Nd(^{3}He, t)^{150}Pm reaction were not available in Ref. [24].

From Fig. 18, it is clear that all three isotopes overlap near 17 MeV. The differences below that energy could be explained by the facts that different nuclei have their Gamow–Teller resonance located at different excitation energies [36] and that deformation effects (^{150}Nd is a deformed nucleus) could influence the distribution of the Gamow–Teller strength. However, at higher excitation energies, the results of the ^{116}Sn target starts to deviate again from the other two. This deviation is still within the error bands. Nevertheless, it could be an interesting feature due to the general quenching phenomenon of the Gamow–Teller strength. This phenomenon is well-documented in the literature [36,37,55,56] and results in that only about 50−60% of the Ikeda sum rule is exhausted by the Gamow–Teller strength in the Gamow–Teller resonance region. Without subtracting the quasi-free background, Guess et al., found $(52 \pm 5)\%$ of the Ikeda sum rule below 28 MeV for the ^{150}Nd target and we found $(48 \pm 6)\%$ for the ^{122}Sn target, both in agreement with this phenomenon. However, for the ^{116}Sn target, we found only $(38 \pm 7)\%$.

The Gamow–Teller distribution where the quasi-free background is not subtracted goes through zero near 20 MeV for the ^{116}Sn target (see Fig. 13). Because of the general shape of the quasi-free background (see Fig. 17 and Eq. (5)), we conclude that the contribution from the quasi-free background to the $\Delta L = 0$ multipolarity contribution is small for the ^{116}Sn target (the only zero-point in Fig. 17 is at $S_p = 4.08$ MeV [18] for this target). Note that due to the large systematic errors, we can only conclude that the contribution is small for the ^{116}Sn target, not that it is exactly zero. On the other hand, the Gamow–Teller distribution for the ^{150}Nd target published in Ref. [24], as well as the Gamow–Teller distribution shown in Fig. 14 (where no quasi-free background was subtracted) do not become zero above the Gamow–Teller resonance. Hence, in those distributions, the contribution from the quasi-free background may be larger.

Unfortunately, it is very difficult to determine the correct contribution from the quasi-free background (the value of N_0 in Eq. (5)) [37]. The reason for this is that the region near 28 MeV may contain Gamow–Teller strength that is moved to higher excitation energies due to 2p–2h couplings [57,58], and it may contain tails from the isovector giant monopole resonance (IVGMR) and the isovector spin giant monopole resonance (IVSGMR) [37]. Since all these contributions are $\Delta L = 0$ and the quasi-free background also has a $\Delta L = 0$ contribution, an MDA cannot distinguish between these contributions (it would give a significant contributing to the systematic uncertainties; see Sect. 3). Therefore, due to the absense of an (almost) zero-point in the region above the Gamow–Teller resonance for the ^{122}Sn and ^{150}Nd [24] targets, there is no reliable method to estimate the quasi-free background contributions for those targets. The contributions may be as small as for the ^{116}Sn target, but they may also be significantly larger. We conclude that the data do not contain enough information to accurately determine the quasi-free contribution. For this reason, Guess et al., chose not to subtract the quasi-free background at all (which is equivalent to putting $N_0 = 0$), so they would be ensured that no Gamow–Teller, IVGMR, and IVSGMR contributions were neglected.

To summarise, we conclude that only $(38 \pm 7)\%$ of the Ikeda sum rule is found for ^{116}Sn, which seems to have little quasi-free background in its spectra, and that the percentages of the Ikeda sum rule measured for the ^{122}Sn and ^{150}Nd isotopes, which may, or may not have a significant quasi-free background contribution in their spectra, agree with the general trend of the quenching phenomenon. However, it should be noted that the percentage of the Ikeda sum rule for the ^{116}Sn target ($(38 \pm 7)\%$) is not necessarily in disagreement with the observed general quenching phenomenon if one considers the large measurement error of 7% (which contains a 6% systematic contribution). This issue raises the need for accurate determination of the quasi-free background contribution, in order to have a better understanding of the quenching phenomenon of the Gamow–Teller strength.

7 Comparison to QRPA+QPVC calculations

The measurements of the ^{116}Sn and ^{122}Sn targets were also compared to Quasi-Particle Random-Phase Approximation with Quasi-Particle Vibration Coupling (QRPA+QPVC) calculations performed with the Skyrme SkM* interaction [59]. For a more detailed discussion of the formalism of QRPA+QPVC calculations, as well as for an application to ^{120}Sn, the interested reader is referred to Ref. [60]. The calculations presented in this section were performed specifically for the present paper.

In the previous section, it was discussed that the quasi-free background contribution is small for the ^{116}Sn target. Therefore, overestimating the subtraction of this quasi-free background could result in losing Gamow–Teller strength at higher excitation energies (2p–2h couplings). For this reason, we chose to compare the calculations to our results where no quasi-free background was subtracted.

Our self-consistent calculations should fulfill, by construction, the Ikeda sum rule. In practise, the QRPA+QPVC calculations reproduce 97% of Ikeda sum rule when the strength is integrated up to an excitation energy of 80 MeV [60]. The inclusion of the QPVC effect could shift 10 − 15% of the Gamow–Teller strength to excitation energies above 25 MeV, however, this is still not enough to fully explain the general quenching phenomenon. Therefore, in order to compare with experimental data, the theoretical calculations were artificially normalised to $(0.75)^2 \cdot 3|N - Z|$, in agreement with Ref. [24]. The comparison is illustrated in Figs. 20 and 21.

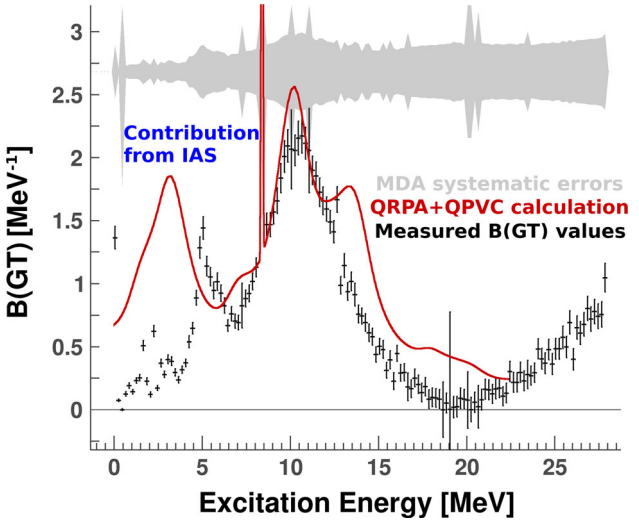

Fig. 20 Comparison between experimental data (measured with (^{3}He, t) at 140 MeV/u) and QRPA+QPVC calculations for the Gamow–Teller strength distribution of ^{116}Sb in the situation where the quasi-free background was not subtracted. Note that higher B(GT) '$\Delta L = 0$' strength could possibly be due to the low-energy tail of the IV(S)GMR ($2\hbar\omega$), which was not included in the calculations

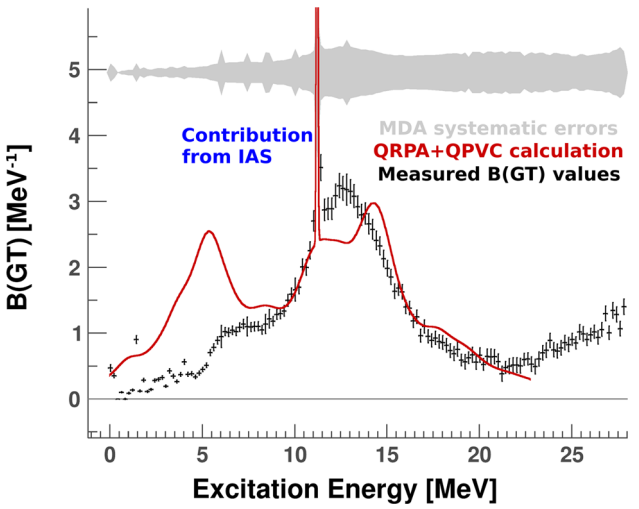

Fig. 21 Same as Fig. 20, but now for ^{122}Sb

From Figs. 20 and 21, we conclude that the QRPA+QPVC calculations were able to reasonably predict the IAS and the Gamow–Teller resonance. If the systematic uncertainties are included, the theoretical result is always within a 2σ distance of the experimental data. However, in the region of 3−5 MeV excitation energy, the QRPA+QPVC calculations show a large, broad peak, which has not been observed experimentally. This peak is the result of the lowest main state of the QRPA+QPVC model, which corresponds to a single-particle excitation of back spin-flip type ($j = l - 1/2 \rightarrow j = l + 1/2$) [60]. Also, the inclusion of attractive isoscalar pairing interactions in the QRPA+QPVC model is partially responsible, as it increases the height of this peak by about 20% (it also improves the agreement with experimental data in the region of the Gamow–Teller resonance) [60]. The peak in the 3−5 MeV region is a known discrepancy between the QRPA+QPVC model and experimental data. It also showed up for ^{120}Sn in Ref. [60]. Possible extensions of the QRPA+QPVC model of Ref. [60] may be envisaged (e.g., by including further correlations). At the same time, the Gamow–Teller peaks result from the interplay of the single-particle spin–orbit splittings and of the residual interaction between particle–hole excitations. Therefore, refinements on the effective interactions to increase their accuracy in this respect should also be investigated, although this may be quite demanding and show the limitations of the present Skyrme ansatz.

Even though the QRPA+QPVC calculations were able to reasonably predict the IAS and the Gamow–Teller resonance, no conclusions about the quasi-free background or the general quenching phenomenon could be drawn from this, which was our hope when making this comparison. Since the calculations satisfy the sum rule when the Gamow–Teller strength up to 80 MeV is integrated, an improvement of the 3−5 MeVregion would increase the strength either in the Gamow–Teller resonance region, or in the excitation-energy region above 25 MeV. This needs to be further checked by a proper effective interaction that can better reproduce the low-energy data. Hence, the current agreement in the region of the Gamow–Teller resonance could be fortuitous. On the other hand, we can conclude from this comparison that the data presented in this paper do provide a useful reference for improving the current theoretical calculations, especially by giving a guideline for the improvement of the spin–isospin terms of the effective interactions in the nuclear medium.

No QRPA+QPVC calculations were done above 22 MeV for this work. We would like to note that in order to extend the calculations to 28 MeV, contributions from the IVGMR, IVSGMR, shifted Gamow–Teller strength and the quasi-free background would all have to be included, because MDA cannot reasonably distinguish between these contributions. Including the quasi-free background in the QRPA+QPVC calculations may be challenging, because the QRPA+QPVC formalism was originally not meant to model this phenomenon. However, from Sect. 6, it follows that the quasi-free background could be significant for some of the isotopes and some quasi-free contribution has to be included in the theoretical calculations if the goal is to achieve agreement with experimental data.

8 Outlook

In Sect. 6, we concluded that more research is required to study the quasi-free background. This is needed to accurately estimate the quasi-free background contributions not only in the data presented in this work, but also in other data.

These data may include what has been presented by Guess et al. [24], so that the general quenching phenomenon of the Gamow–Teller resonance can be better understood.

A possibility would be to repeat the measurements of this work, the ^{116}Sn(^{3}He, t)^{116}Sb and ^{122}Sn(^{3}He, t)^{122}Sb reactions at 140 MeV/u, while measuring the proton emissions at backward angles. The requirement of a coincidence between emitted tritons at forward angles and emitted protons at backward angles has proven to be a powerful technique to suppress the quasi-free background [37]. However, it should be noted that this will also reduce the Gamow–Teller strength distributions, because states that cannot decay by proton emission will be removed from the distribution.

Therefore, it would be a better strategy to measure the proton emissions of the recoil nucleus over the full 4π solid angle. It is known from Ref. [37,61] that the quasi-free background corresponds almost exclusively to protons emitted in the forward hemisphere (with respect to the recoil axis). On the other hand, in the LAB-frame, all multipole distributions have a symmetric distribution in the forward and backward hemisphere with respect to the recoil axis. Hence, if one would integrate the measured data over these two hemispheres and subtract the two, all multipole contributions to proton decay should cancel out and only the contribution from the quasi-free background should remain. This remaining quasi-free background contribution can be used to directly determine N_0 in Eq. (5). This is because the quasi-free background in Figs. 13 and 14 is due to charge-exchange knock-on proton emission. The only uncertainly may come from the small quasi-free contribution that might still be present in the backward hemisphere.

With such an experiment, it would be possible to confirm that the quasi-free contribution to the $\Delta L = 0$ component of the ^{116}Sn(^{3}He, t)^{116}Sb reaction at 140 MeV/u is indeed small. The experiment can also be used to see whether a proper subtraction of the quasi-free background (which is only possible when N_0 is known) results in a better agreement between the Ikeda sum rule percentages of the two Sn-targets. However, it should be noted that the experiment described above to measure N_0 might be challenging. The reason for this is that the proton emission is generally expected to be very strong at forward angles, which leads to very high count rates in the solid-state detectors. Moreover, at these forward angles the detectors are also expected to be bombarded by products of other nuclear reactions than the one of interest.

A QRPA+QPVC calculation with the inclusion of contribution from excitations of other multipolarities up to 28 MeV/u would also be helpful to better understand the general quenching phenomenon. For this purpose, the calculation would have to be extended to higher excitation energies, and contributions from the IVGMR, IVSGMR and shifted Gamow–Teller strength would have to be included to allow for a good comparison with experimental data.

9 Concluding remarks

The Gamow–Teller strength distributions of ^{116,122}Sn $\rightarrow$ ^{116,122}Sb were measured with the (^{3}He, t) charge-exchange reaction at a bombarding energy of 140 MeV/u. The results were compared with the same distributions obtained in previous measurements at a lower incident energy of 67 MeV/u. When the same analysis procedure was applied, we found agreement, which confirms the reliability of the new measurements. However, the old analysis procedure showed several inaccuracies, and we improved the analysis method (see Sect. 3 for the description of the new method).

The data (with the new analysis method) were also compared to ^{150}Nd $\rightarrow$ ^{150}Pm data and to QRPA+QPVC calculations. Without subtracting the quasi-free background, we found $(48 \pm 6)\%$ of the Ikeda sum rule in the region below an excitation energy of 28 MeV for the ^{122}Sn target. This agrees with the general trend of the quenching phenomenon of the Gamow–Teller strength. For the ^{116}Sn target, we found $(38 \pm 7)\%$ in the same excitation-energy region, which appears to be somewhat lower (the errors include all systematic uncertainties). These summed Gamow–Teller strengths were extracted as usual by using the unit cross section in the region up to an excitation energy of 28 MeV, well above the main Gamow–Teller resonance, after extrapolating the cross sections to $q = 0$.

Our comparisons suggest that there could be a difference in the amount of quasi-free background that is present for both Sn-targets. The quasi-free background contribution is believed to be small for the ^{116}Sn target, but may, or may not be larger for the ^{122}Sn target. The present data for the ^{122}Sn target are inconclusive about this. When the largest possible quasi-free background contribution was subtracted [22], we found $(29 \pm 7)\%$ ($(35 \pm 5)\%$) of the Ikeda sum rule for the ^{116}Sn (^{116}Sn) target in the same excitation-energy region.

From these numbers, we conclude that more research is needed to better understand the general quenching phenomenon. From the experimental side, measurement techniques are needed to determine the size of the quasi-free background. From the theoretical side (once the quasi-free background contribution is established), more investigations are necessary to determine whether the lower percentage of the ^{116}Sn target indeed is in disagreement with the general trend of the quenching phenomenon.

10 Authors' contributions

CAD has written the first draft of the manuscript, based on his PhD thesis [23]. CAD also has done the data analysis (Sect. 3) under the supervision of MNH and NK-N. The raw data can be requested at RCNP [17]. The experiment was originally proposed by HA, HE, DF and MNH. HA, GC,

HE, MNH, NK-N, YFN, AT and RGTZ all have provided significant contributions to the discussion and interpretation of the results (Sects. 4–7), and they were also involved in improving the first draft into the final manuscript. RGTZ has also provided important supervision in the MDA part of the analysis. The QRPA+QPVC calculations (Figs. 20 and 21) were provided by GC and YFN. All authors except RGTZ, GC and YFN were involved in the preparation and execution of the experiment. All authors have read the manuscript and agreed with its publication.

Acknowledgements We wish to thank the operators of the Research Center for Nuclear Physics, Osaka University, Ibaraki, Osaka, 567-0047, Japan for operating the measurement equipement and, therefore, providing a crucial contribution to the experiment. This work was supported by the US National Science Foundation (NSF) under Cooperative Agreement PHY-156554 (NSCL) and PHY-1430152 (JINA Center for the Evolution of the Elements). This work was also supported by DFG Grant SFB1245 and German BMBF Grant 05P19RDFN1.

Data Availability Statement This manuscript has no associated data or the data will not be deposited. [Authors' comment: This manuscript has no associated data with it because of Computer Memory limitations (the data is hundreds of GB). The raw data used in the analysis can be requested at RCNP [17].]

References

1. D. Frekers et al., Nucl. Phys. A **916**, 219 (2013)
2. W.T. Chou et al., Phys. Rev. C **47**, 163 (1993)
3. G. Perdikakis et al., Phys. Rev. C **83**, 054614 (2011)
4. J.D. Vergados et al., Rep. Prog. Phys. **75**, 106301 (2012)
5. H. Ejiri, Phys. Rep. **338**, 265 (2000)
6. H. Ejiri et al., Phys. Rep. **797**, 1 (2019)
7. D. Frekers, M. Alanssari, Eur. Phys. J. A **54**, 177 (2018)
8. H. Ejiri et al., Phys. Lett. B **729**, 27 (2014)
9. J.D. Vergados, Phys. Rep. **361**, 1 (2002)
10. T. Brunner, L. Winslow, Nucl. Phys. News **27**, 14 (2017)
11. K. Langanke, G. Martinez-Pinedo, Rev. Mod. Phys. **75**, 819 (2003)
12. A. Arcones et al., Prog. Part. Nucl. Phys. **94**, 1 (2017)
13. H. Schatz, J. Phys. G Nucl. Part. Phys. **43**, 064001 (2016)
14. M. Fujiwara et al., Phys. Rev. Lett. **85**, 4442 (2000)
15. A. P. Severyukhin, H. Sagawa, Prog. Theor. Exp. Phys. **2013**, 103D03 (2013). https://doi.org/10.1093/ptep/ptt085
16. M. Fujiwara et al., Nucl. Instr. Meth. Phys. Res. A **422**, 484 (1999)
17. RCNP (2019), http://www.rcnp.osaka-u.ac.jp/index_old.html. Accessed 14 Jan 2019
18. C. L. Dunford, T.W. Burrows, NNDC Informal Report NNDC/ONL (2018), https://www.nndc.bnl.gov/
19. RCNP Collaboration, *Using high resolution* (^{3}He, *t*) *reactions on* ^{116}Cd *for nuclear and neutrino physics*, Proposal for an experiment at RCNP (2014)
20. RCNP Collaboration, *High energy-resolution study of the* (^{3}He, t) *reactions on* Ge, Sn *and* Te *isotopes at* 420MeV *and* SD 2^- *neutrino responses*, Proposal for an experiment at RCNP (2014)
21. R.G.T. Zegers et al., Phys. Rev. Lett. **99**, 202501 (2007)
22. K. Pham et al., Phys. Rev. C **51**, 526 (1995)
23. C. A. Douma, Ph.D. thesis, University of Groningen (2019), https://www.rug.nl/research/portal/files/74454235/Complete_thesis.pdf
24. C.J. Guess et al., Phys. Rev. C **83**, 064318 (2011)
25. Atsushi Tamii, Ph.D. thesis, Kyoto University (1999), https://m.kulib.kyoto-u.ac.jp/webopac/TD00030077
26. T. Wakasa et al., Nucl. Instr. Meth. Phys. Res. A **482**, 79 (2002)
27. H. Fujita et al., Nucl. Instr. Meth. Phys. Res. A **484**, 17 (2002)
28. H. Fujita et al., Nucl. Instr. Meth. Phys. Res. A **469**, 55 (2001)
29. R.G.T. Zegers et al., Phys. Rev. C **78**, 014314 (2008)
30. R. Brun, F. Rademakers, Nucl. Instr. Meth. Phys. Res. A **389**, 81 (1997)
31. G. Gey, Private Communication (2019)
32. H. Fujimura et al., Phys. Rev. C **69**, 064327 (2004)
33. H. Matsubara, Ph.D. thesis, Department of Physics, Graduate School of Science, Osaka University, Japan (2010), http://www.rcnp.osaka-u.ac.jp/Divisions/np1-a/thesis/Matsubara_PhD2010.pdf
34. C. A. Douma et al., *Measurement of the Gamow-Teller strength in* ^{116}Sn *and* ^{122}Sn *in the* S452 *experiment*, RCNP Annual Report (2016)
35. J. Lilley, *Nuclear Physics, Principles and Applications*. (Wiley, Hoboken, 2001)
36. M.N. Harakeh, A. van der Woude, *Giant Resonances: Fundamental High Frequency Modes of Nuclear Excitation, Oxford Studies in Nuclear Physics* (Clarendon Press, Oxford, 2001)
37. R. G. T. Zegers, Ph.D. thesis, University of Groningen (1999), http://hdl.handle.net/11370/087b6413-b9de-4e65-9127-35f60da42a1d
38. J. Cook, J. A. Carr, Computer Program FOLD (1982)
39. F. Petrovich, D. Stanley, Nucl. Phys. A **275**, 487 (1977)
40. J. Cook et al., Phys. Rev. C **30**, 1538 (1984)
41. R. G. T. Zegers et al. Computer Program FOLD (2006)
42. M.A. Hofstee et al., Nucl. Phys. A **588**, 729 (1995)
43. S. Y. van der Werf, Computer Program NORMOD (2019)
44. J. Guillot et al., Nucl. Phys. A **752**, 349 (2005)
45. D.Y. Pang et al., Phys. Rev. C **79**, 024615 (2009)
46. P. Puppe et al., Phys. Rev. C **86**, 044603 (2012)
47. J. Kamiya et al., Phys. Rev. C **67**, 064612 (2003)
48. T. Yamagata et al., Nucl. Phys. A **589**, 425 (1995)
49. S.Y. van der Werf et al., Nucl. Phys. A **496**, 305 (1989)
50. J. Jänecke et al., Phys. Rev. C **48**, 2828 (1993)
51. R.G.T. Zegers et al., Phys. Rev. C **74**, 024309 (2006)
52. G.W. Hitt et al., Phys. Rev. C **80**, 014313 (2009)
53. B.S. Flanders et al., Phys. Rev. C **40**, 1985 (1989)
54. T.N. Taddeucci et al., Nucl. Phys. A **469**, 125 (1987)
55. C. Gaarde, Nucl. Phys. A **396**, 127 (1983)
56. J. Rapaport, E. Sugarbaker, Ann. Rev. Nucl. Part. Sci. **44**, 109 (1994)
57. T. Wakasa et al., Phys. Rev. C **55**, 2909 (1997)
58. M. Ichimura et al., Prog. Part. Nucl. Phys. **56**, 446 (2006)
59. J. Bartel et al., Nucl. Phys. A **386**, 79 (1982)
60. Y.F. Niu et al., Phys. Rev. C **94**, 064328 (2016)
61. H. Akimune et al., Phys. Lett. B **323**, 107 (1994)